Saddle-like topological surface states on the $TT'X$ family of compounds (T, T' = Transition metal, X = Si, Ge)

Bahadur Singh,[1,2,*] Xiaoting Zhou,[1,2] Hsin Lin,[1,2,†] and Arun Bansil[3]

[1]*Centre for Advanced 2D Materials and Graphene Research Centre, National University of Singapore, Singapore 117546*
[2]*Department of Physics, National University of Singapore, Singapore 117542*
[3]*Department of Physics, Northeastern University, Boston, Massachusetts 02115, USA*

Topological nodal-line semimetals are exotic conductors that host symmetry-protected conducting nodal lines in their bulk electronic spectrum and nontrivial drumhead states on the surface. Based on first-principles calculations and an effective model analysis, we identify the presence of topological nodal-line semimetal states in the low crystalline symmetric $TT'X$ family of compounds (T,T' = transition metal, X= Si or Ge) in the absence of spin-orbit coupling (SOC). Taking ZrPtGe as an exemplar system, we show that owing to small lattice symmetry this material harbors a single nodal line on the $k_y = 0$ plane with large energy dispersion and unique drumhead surface state with a saddlelike energy dispersion. When the SOC is included, the nodal line gaps out and the system transitions to a strong topological insulator state with $Z_2 = (1; 000)$. The topological surface state evolves from the drumhead surface state via the sharing of its saddlelike energy dispersion within the bulk energy gap. These features differ remarkably from those of the currently known topological surface states in topological insulators such as Bi_2Se_3 with Dirac-cone-like energy dispersions.

I. INTRODUCTION

Recent discovery of nontrivial band structures in semimetals has prompted prodigious research interest in topological semimetals [1–17]. Unlike topological insulators (TIs), the protected gapless states of which live only on their surfaces, topological semimetals (TSMs) feature unusual crystal-symmetry-protected states both in the bulk as well on the surface. In particular, the bulk Fermi surfaces of TSMs enclose nontrivial band-touching points that bring quantized numbers for integrals of the Berry flux over any closed surface enclosing these points, and provide the relevant topological invariants. Depending on band degeneracy and the momentum-space distribution of the band-touching points, three different types of TSMs, namely, Weyl semimetal (WSM)[5–10], Dirac semimetal (DSM) [11,12], and nodal-line semimetal (NLSM) [13–17], have been proposed. WSMs and DSMs exhibit two- and fourfold band-touching points with low-energy Weyl and Dirac fermion excitations, respectively, with zero-dimensional Fermi surfaces in the three-dimensional bulk Brillouin zone (BZ). In sharp contrast to WSMs and DSMs, NLSMs support extended band-touching points along a line with one-dimensional Fermi surfaces in the bulk BZ. WSMs have been found in noncentrosymmetric TaAs [9,10], $Mo_xW_{1-x}Te_2$ [18–20], and LaAlGe [21] families, while DSMs have been realized in Na_3Bi [11] and Cd_2As_3 [12].

Among the TSMs, NLSMs offer many unique properties that are distinct from WSMs and DSMs [14–17,22–24]. For example, NLSMs have higher density of states (DOS) at the Fermi level than DSMs and WSMs, and therefore provide an ideal platform to study interaction-induced instabilities. They also feature topological surface states (TSSs), known as drumhead surface states (DSSs), which could be interesting for achieving superconductivity and correlation physics [23–25]. Despite much theoretical effort [26–34], the experimental evidence for NLSMs has been only reported recently for ZrSi(S,Te) [35,36], $PbTaSe_2$ [37], and $PtSn_4$ [38]. A focus of discussion has been the issue of the stability of nodal lines in the absence of spin-orbit coupling (SOC) effects [16,17,26–29]. Turning on the SOC either splits the nodal line into nodal points, depending on crystalline symmetries present [7,8,26,27], or fully gaps the spectrum due to hybridization with bands of same symmetry [28,29,34–36]. Regardless, saddlelike TSSs have not been found in these materials.

In this paper, we identify topological nodal-line fermion states in the large family of silicides or germanides $TT'X$ (T,T' = transition metal, X= Si or Ge) when the SOC is ignored. Taking ZrPtGe as an explicit example, we show that a single nodal line lies on the $k_y = 0$ bulk plane and a saddlelike DSS is nested inside the nodal line projection on the (010) surface. Inclusion of the SOC gaps the nodal line, realizing a Z_2 nontrivial topological state with $Z_2 = (1; 000)$. The TSS evolves from the DSS with similar saddlelike energy dispersion. This is very unique since the known TIs such as Bi_2Se_3 have Dirac-cone-like surface states [39,40]. It is well known that saddle points in the band structure give rise to interesting saddle-point van Hove singularities (VHSs) where the two-dimensional (2D) density of states diverges [41]. When the VHS lies close to the Fermi level, the instabilities among lattice, charge, and spin degrees of freedom as well as superconducting transition temperature, ferromagnetism, and/or antiferromagnetism are substantially enhanced even in
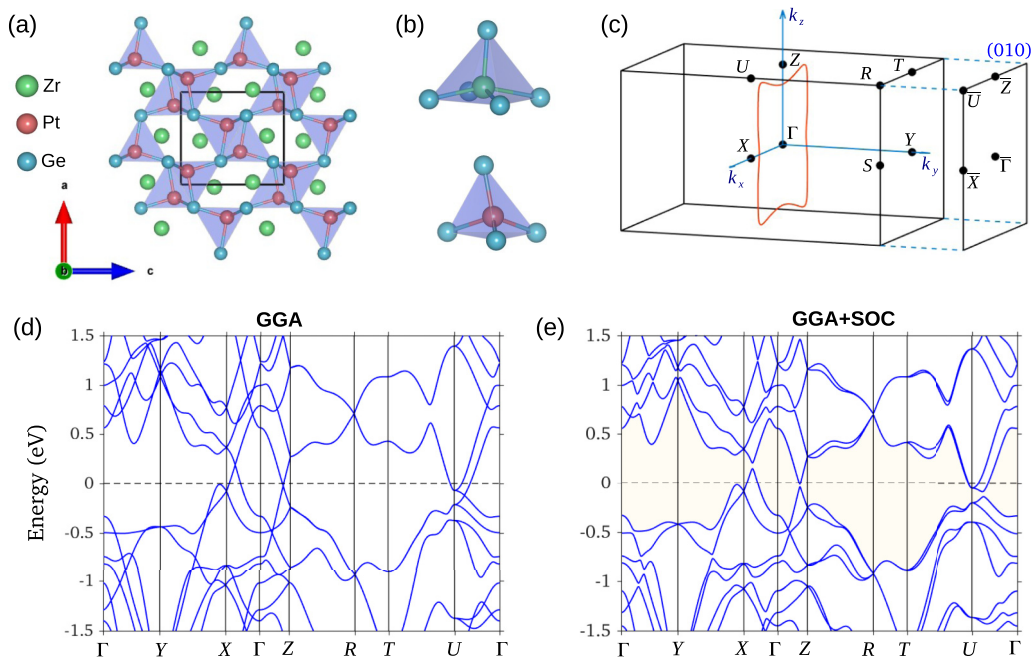
---

*bahadursingh24@gmail.com
†nilnish@gmail.com

FIG. 1. (a) Crystal structure of ZrPtGe with *Pnma* symmetry. (b) Local coordination of the Zr (top panel) and Pt (bottom panel) atoms in the unit cell. (c) Bulk Brillouin zone and its projection on the (010) surface. The relevant high-symmetry points are marked with black dots. The calculated momentum distribution of the nodal line is shown with orange on the $k_y = 0$ plane. (d) Bulk band structure without spin-orbit coupling (SOC). Band crossings are evident along the $\Gamma - X$, $\Gamma - Z$, and $\Gamma - U$ directions near the Fermi level. (e) Bulk band structure with SOC. A small band gap opens at the band-crossing points. The shaded region highlights the continuous gap below which the topological invariants are calculated.

the weak-coupling limit [42–47]. Our proposal of NLSM with saddlelike TSSs in the large family of silicides and germanides therefore provides an exciting materials platform to explore these exotic properties in the presence of a nontrivial band topology.

II. METHOD AND CRYSTAL STRUCTURE

We performed electronic structure calculations with the projector augmented wave method [48–50] and generalized gradient approximation (GGA) [51], using VASP [49]. SOC was included in calculations self-consistently. The surface energy dispersions were calculated within the tight-binding scheme, using the WannierTools [52–54].

The $TT'X$ compounds considered all crystallize in an orthorhombic Bravais lattice with the nonsymmorphic space group D_{2h}^{16} (*Pnma*, no. 62) [55,56]. The crystal structure of ZrPtGe is illustrated in Fig. 1(a) as an example. In this structure, Pt and Ge atoms form a strongly corrugated Pt_3Ge_3 hexagonal network and Zr atoms fill the cavities left in the network. Due to strong puckering between different atomic layers, Pt forms a distorted tetrahedral configuration with Ge whereas Zr is coordinated with five Ge atoms as seen in Fig. 1(b). The first orthorhombic bulk and (010) surface BZs with the relevant high-symmetry points are shown in Fig. 1(c).

III. ELECTRONIC STRUCTURE

The electronic structure of ZrPtGe without the SOC [Fig. 1(d)] unveils its semimetallic ground state. The valence and conduction bands are seen to cross along the high-

symmetry lines $\Gamma - X$, $\Gamma - Z$, and $\Gamma - U$ that are tied to the $k_y = 0$ plane of the bulk BZ. A full BZ exploration shows that these band crossings persist along a closed path, realizing a single nodal line on the $k_y = 0$ plane inside the bulk BZ as shown in Fig. 1(c). When we include the SOC, the nodal line evaporates with the opening of a gap at the band-crossing points [Fig. 1(e)]. It should be noted that owing to the coexistence of inversion (P) and time reversal symmetry (Θ) each band still remains doubly degenerate in the presence of the SOC at each k point. Furthermore, additional nonsymmorphic crystalline symmetries in this system lead to fourfold band crossings at the BZ boundary planes ($k_i = \pi$) above and below the Fermi level. These band crossings are protected against gap opening and may realize high-symmetry Dirac cones at X, Y, and Z points. The energy dispersion can be tuned by changing the transition-metal elements in the system as shown in Appendix E.

In order to characterize the nature and the topological protection of the nodal line, we systematically examine the band crossings in Fig. 2. We know that the nodal line resides on the $k_y = 0$ plane, which is a $M_y : (x,y,z) \rightarrow (x,-y,z)$ mirror invariant plane. Each band on this plane can have a well-defined M_y mirror eigenvalue. If a band crossing happens between two bands of different eigenvalues, it can remain gapless. Figure 2(a) shows the bands along two principal directions on the $k_y = 0$ plane and the corresponding mirror eigenvalues in the absence of the SOC. Note that we have obtained M_y eigenvalues from our first-principles Bloch wave functions and since the Hamiltonian remains spin-rotation invariant without SOC it has eigenvalues $+1$ or -1. Clearly, the lowest conduction band and the highest valence band have different mirror eigenvalues and thus their crossing points are
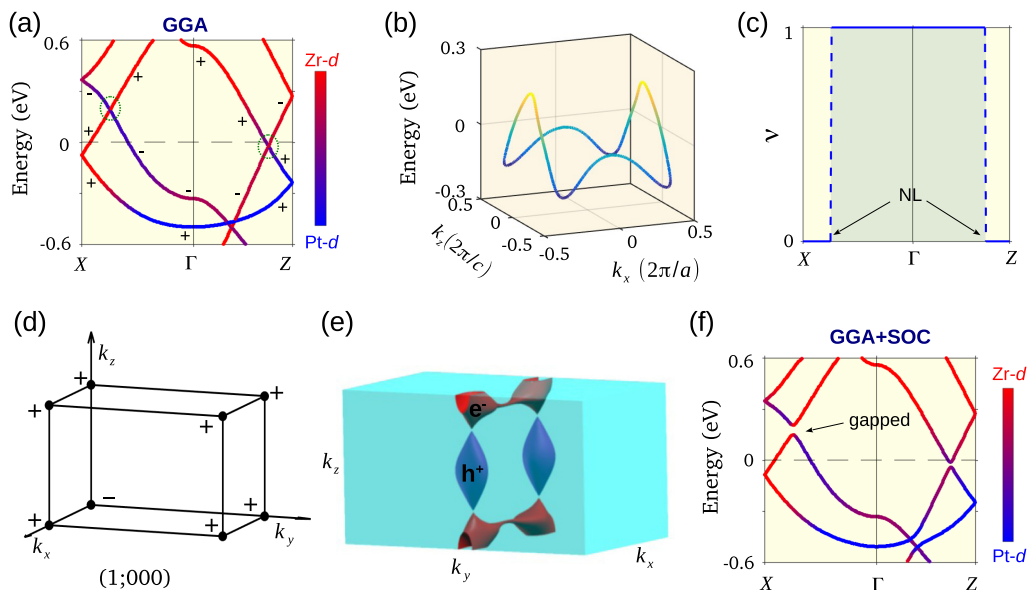
FIG. 2. (a) Orbital compositions and mirror eigenvalues of the bulk bands without SOC. (b) Energy-dependent nodal line configuration on the $k_y = 0$ plane. (c) Variation of the nontrivial topological invariant along the high-symmetry lines in the bulk Brillouin zone. The topological invariant is calculated using M_y mirror eigenvalues of the occupied bands on the mirror symmetric $k_y = 0$ and π planes without SOC. (d) Products of parity eigenvalues of the occupied bands at eight time-reversal-invariant k points in the bulk BZ and the related Z_2 indices without SOC. (e) The Fermi surface with electron (red) and hole (violet) pockets. (f) Orbital compositions of the bulk bands with SOC. A small band gap opens at the band crossings.

topologically protected against gap opening. Further analysis of orbital characters shows that bands around the Fermi level are dominated by Pt and Zr d states with a clear signature of band inversion at the Γ point [Fig. 2(a)]. We explicitly calculated the topological invariant for the system using the mirror eigenvalue analysis [28,29]. The computed topological invariant ν takes nontrivial value only inside the nodal line [Fig. 2(c)] and thus signals the existence of an odd number of DSSs inside the nodal line projection over the surface [28,29].

The topological stability can be further assessed by calculating the topological invariants $Z_2 = (\nu_0; \nu_1 \nu_2 \nu_3)$ defined in the presence of P and Θ symmetries without the SOC [26]. Our calculations yield a nontrivial $Z_2 = (1; 000)$ [see Fig. 2(d)]. This result demonstrates that the nodal line in ZrPtGe is also protected by P and Θ. In Fig. 2(b), we present the nodal-line structure in the $E - k_x - k_z$ space. The nodal line is seen to exhibit a substantial energy dispersion around the Fermi level with the corresponding energies of 0.189, -0.023, and -0.119 eV along k_x, k_z, and the plane diagonal to the ($k_x - k_z$) directions. The large energy dispersion of the nodal line results in a unique Fermi surface that constitutes compensated electron and hole pockets as shown in Fig. 2(e).

Figure 2(f) illustrates the energy bands with SOC. In general SOC can drive NLSMs into DSM, WSM, or a fully gapped insulator. However, in view of the lowered crystalline symmetries of ZrPtGe, the SOC opens a full gap at the crossing points, making the conduction and valence band separate at each k point. Since the nodal line winds around a single time-reversal invariant point (Γ) with a nontrivial band topology, the SOC drives the system into a nontrivial insulating state with $Z_2 = (1; 000)$ (see Appendix B for details).

To further showcase the protected surface states and their connection to bulk nodal lines, we present these states for the semi-infinite (010) surface in Fig. 3. The bulk bands projected onto the (010) surface without the SOC are shown in Fig. 3(a) where the nodal-line crossings can be clearly seen. The DSSs nested inside the nodal line are visible in Fig. 3(b), which is consistent with the calculated nontrivial invariant inside the nodal line. Unlike the nearly flat DSSs reported in earlier works [26–29], the states in ZrPtGe are more dispersive, and interestingly they have opposite band curvatures along the $\overline{\Gamma} - \overline{X}$ and $\overline{\Gamma} - \overline{Z}$ directions, realizing a unique saddlelike energy dispersion.

Figures 3(c) and 3(d) show (010)-projected bulk bands and surface bands, respectively, with the SOC. The nodal line is now gapped and the DSS splits away from the time-reversal invariant $\overline{\Gamma}$ point, deforming into a topological Dirac-cone state. Since the SOC here is much smaller than the dispersion of the DSS, the upper and lower branches of the TSS display the same band curvatures or carrier velocities. Furthermore, these states retain the saddlelike features of the DSS energy dispersion, which is more clearly visible in the Fermi band contours shown in Figs. 3(e)–3(g). The constant energy contours (CECs) are seen to be open and disperse along the k_x direction above the Dirac point or the saddle point. As we lower the Fermi energy, the electronic states undergo a Lifshitz transition and the CECs change direction and dispersion to lie along the k_z direction.

We want to emphasize that TSSs with saddlelike energy dispersion are unique to the ZrPtGe family. They are symmetry allowed (see below) and their characteristic saddlelike dispersion is controlled by their bulk nodal-line structure. Therefore, we should expect these states to be robust over a range of different surface potentials, although details of their energy positions can be shifted via changes in surface potentials (see Appendix C for details). In particular, we have found that when we repeat our computations using the more advanced
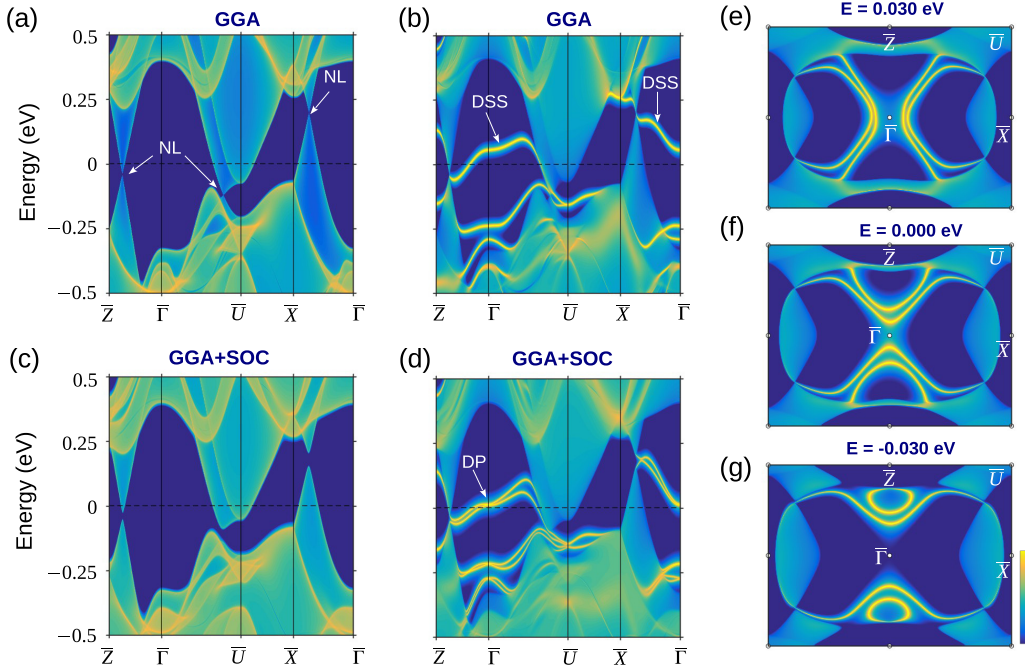
FIG. 3. (a) Projected bulk bands onto the (010) surface without SOC. The nodal line (NL) crossings are shown with arrows. (b) Band structure of the (010) surface without SOC. The nontrivial drumhead surface states (DSSs) are marked with arrows. (c, d) Same as (a) and (b) but with the SOC included. The nontrivial surface states evolve from the DSSs with different band curvatures along different high-symmetry directions. The Dirac point (DP) is identified with the arrow. Isoenergy-band contours at (e) $E = 0.030$ eV, (f) $E = 0.000$ eV, and (g) $E = -0.030$ meV with SOC.

Heyd-Scuseria-Ernzerof (HSE) exchange-correlation functional to obtain the bulk and surface spectrum, the dispersive nature of the bulk nodal line as well as the saddlelike TSSs remain preserved (see Appendix A).

IV. LOW-ENERGY EFFECTIVE MODEL

In order to better understand the saddlelike TSSs, we now present a low-energy effective model Hamiltonian using the theory of invariants in a manner similar to the case of Bi$_2$Te$_3$ [40]. On the (010) surface, in addition to Θ, the only other preserved symmetry is the glide-mirror symmetry $\overline{M}_z = \{M_z | \frac{1}{2} 0 \frac{1}{2}\}$, which sends $(k_x, k_z) \rightarrow (k_x, -k_z)$. Based on our first-principles results and a symmetry analysis, a single-band $\boldsymbol{k} \cdot \boldsymbol{p}$ model Hamiltonian for the DSSs in the absence of the SOC takes the form

$$H_0(k_x, k_z) = \frac{1}{2m^*}\left(k_x^2 - \eta k_z^2\right)$$
$$= -\frac{1}{2m^*}\left[\frac{\eta + 1}{4}\left(k_+^2 + k_-^2\right) + \frac{\eta - 1}{2}k_+ k_-\right],$$
(1)

where $k_\pm = k_z \pm i k_x$. Here coefficient η describes the form of the $E - K$ dispersion and depends on the rotational symmetries and materials properties of the system. While $\eta < 0$ gives a parabolic energy dispersion, $\eta > 0$ ensures a saddlelike energy dispersion (see Appendix D for details). The n-fold rotational symmetry C_n for $n > 2$ normal to the surface in a system forbids $\eta > 0$ since it requires $\eta = -1$, i.e., a saddlelike energy dispersion for the surface state, whereas for $n \leqslant 2$ this is allowed. We have verified this point from symmetry constraints of C_n on the Hamiltonian $H_0(k_x, k_z)$

with $\eta > 0$. Since C_n sends $k_\pm \rightarrow k_\pm e^{\pm i \frac{2\pi}{n}}$ and $(k_+^2 + k_-^2) \rightarrow (k_+^2 e^{i \frac{4\pi}{n}} + k_-^2 e^{-i \frac{4\pi}{n}})$, this Hamiltonian remains invariant only for C_n with $n \leqslant 2$. Notably, this is only a necessary condition for realizing a saddlelike energy dispersion as material properties are also involved in achieving such a dispersion. As ZrPtGe exhibits a substantial nodal-line dispersion in the bulk and its (010) surface lacks C_{ny} with $n > 2$, it hosts a symmetry allowed saddlelike state as found in our results [see Fig. 3]. The energy dispersion associated with the model Hamiltonian (1) is presented in Figs. 4(a)–4(c), which show a saddlelike energy dispersion for the DSS with a single saddle point at the Γ point. The DOS is logarithmically diverging at the Γ point, confirming that it has a saddle-point VHS.

In the presence of SOC, the DSS splits into two branches, developing into the spin-polarized surface states of a strong Z_2 TI. A two-band $\boldsymbol{k} \cdot \boldsymbol{p}$ Hamiltonian is therefore necessary for describing these states. Considering $\overline{M}_z = -e^{-i(k_x - k_z)/2} i \sigma_z$ and $\Theta = i \sigma_y K$, where $\sigma_{i=x,y,z}$ denote Pauli spin matrices, and K is the complex conjugate operator, the effective model Hamiltonian with SOC can be written as

$$H_{\text{SOC}}(k_x, k_z) = \frac{1}{2m^*}\left(k_x^2 - \eta k_z^2\right) + v_k(k_z \sigma_x - k_x \sigma_z) - v_k' k_z \sigma_y,$$
(2)

where $v_x = v_k = v_0(1 + \alpha k^2)$ and $v_z = \sqrt{v_k^2 + v_k'^2} = v_{z0}(1 + \alpha k^2)$ are the Dirac velocities along the x and z axis, respectively, with a second-order correction. The corresponding energy dispersion $E_\pm(\mathbf{k})$ is

$$E_\pm(\mathbf{k}) = \frac{1}{2m^*}\left(k_x^2 - \eta k_z^2\right) \pm \sqrt{v_x^2 k_x^2 + v_z^2 k_z^2}.$$
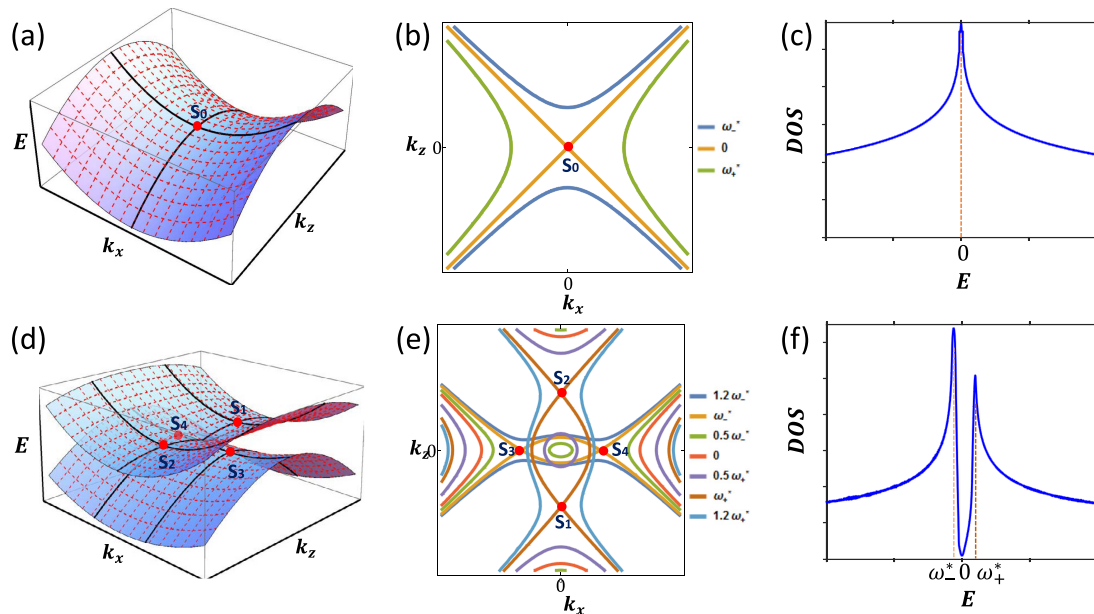(3)

FIG. 4. (a) Energy dispersion of the Hamiltonian $H_0(k_x, k_z)$ with $\eta = +1$, and (b) the associated isoenergy-band contours without SOC. A single saddle point S_0 of the DSS lies at the Γ point. See main text for the meaning of energy-band contours ω_+^* and ω_-^*. (c) Calculated density of states (DOS) for the surface states using the model Hamiltonian [Eq. (1)]. (d),(e) Same as (a) and (b) but with the SOC included. Four saddle points away from Γ (S_1, S_2, S_3, and S_4) emerge due to band splittings in the presence of the SOC. (f) DOS for the surface states with SOC [Eq. (2)].

The preceding energy dispersion demonstrates a type of symmetry-allowed TSS which is distinct from surface states studied so far [1,2]. This TSS evolves from a saddlelike DSS with a single Dirac point at Γ and two pairs of saddle points at generic k points. The two saddle points are located at $(k_x, k_z) = (\pm m^* v_x, 0)$ with energy $\omega_-^* = -\frac{m^* v_x^2}{2}$ on the lower branch while the other two points lie at $(k_x, k_z) = (0, \pm m^* v_z/\eta)$ with energy $\omega_+^* = \frac{m^* v_z^2}{2\eta}$ on the higher branch of the TSS [see Figs. 4(d)–4(f)]. This can be further seen in the DOS [Fig. 4(f)] where the two saddle-point VHSs are evident at ω_-^* and ω_+^*. Such VHSs which appear because of the saddle points at generic k points are classified as type-II VHSs [46].

V. DISCUSSION

The exotic TSSs with VHSs that we have delineated in this paper would provide a platform for exploring the interplay between topological states and strong correlation physics and the related interaction-driven instabilities. For example [46], a type-II VHS system can favor the odd-parity pairing and lead to unconventional superconductivity via weak repulsive interactions. Also, the generic competing orders such as the "valley" charge imbalance, density wave orders (through enhanced nesting via a uniaxial pressure, for example), and superconductivity could possibly be driven by electron-electron interactions [23–25,42–47]. It should be emphasized, however, that the actual ground state realized by a specific material will be influenced by details of the location of the chemical potential, nesting properties, and the nature of the various interactions involved and their relative strengths.

The transition-metal silicides and germanides have been explored in connection with a search for new high-temperature superconductors in the intermetallics. In particular, a number of the materials we have proposed here have been synthesized as single crystals [55–58]. Since our predicted exotic states lie close to the Fermi level, these states could of course be probed directly via angle-resolved photoemission spectroscopy experiments. Moreover, the proposed materials feature unique bulk Fermi surfaces, which may, for example, lead to balanced electron-hole resonance conditions, and thus induce unusual transport characteristics such as a large positive unsaturated magnetoresistance [20].

In summary, our first-principles computations predict that the orthorhombic $TT'X$ family of silicides and germanides harbors a single topologically protected nodal line on the $k_y = 0$ plane in the absence of the SOC. We have demonstrated the existence of DSSs nested inside the nodal line on the (010) surface of ZrPtGe as an exemplar system, which hosts a unique symmetry-allowed saddlelike energy-momentum dispersion relation. Inclusion of the SOC gaps the nodal line and eventually drives the material into the TI phase. The nontrivial TSSs evolve from the DSS and retain their saddlelike energy dispersion and support two pairs of saddle-point VHSs. Our results establish that the $TT'X$ materials family provides an ideal platform for exploring unique physics, including symmetry-breaking quantum states, related with the NLSMs and the saddlelike topological surface states.
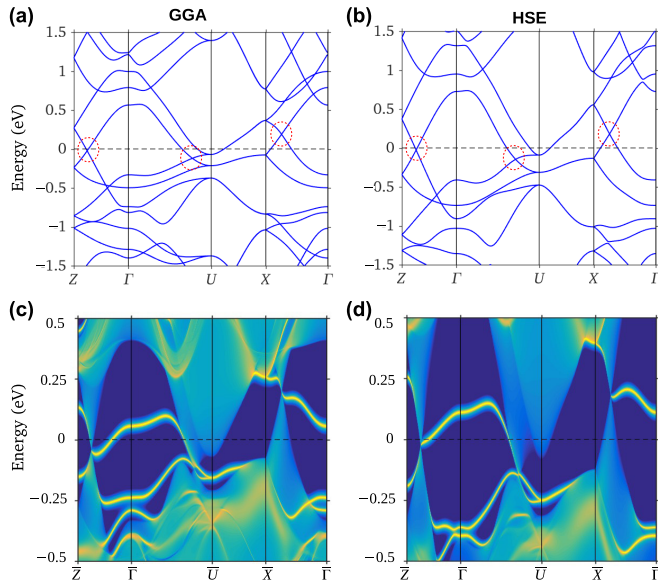
FIG. 5. Band structure of ZrPtGe without SOC. (a) The GGA band structure showing the nodal-line semimetal state. (b) The HSE band structure. The nodal-line crossings along the high-symmetry lines are highlighted with broken-red circles and remain intact after the band-gap correction. Band structure of the (010) surface obtained using (c) GGA and (d) HSE functional. The nontrivial drumhead surface states (DSSs) and their saddlelike energy dispersion maintained with the HSE functional.

APPENDIX A: BAND-GAP CORRECTION

It is well known that the GGA usually underestimates band gaps and results in an overestimation of the band inversion strength. In order to check the robustness of our band inversion and the nodal-line semimetal state in ZrPtGe, we also carried out computations using the more advanced HSE exchange-correlation functional [59], which yields improved band gaps in closer agreement with experiments. Figure 5(a) shows the band structure of ZrPtGe obtained using the GGA, which is the band structure presented also in the main text. The nodal-line band crossings are highlighted with broken red circles. Figure 5(b) gives the band structure based on the HSE functional, where although the band gaps at high-symmetry points are slightly enlarged, the overall features of the GGA band structure are seen to be retained. These results demonstrate that the topological properties and nodal-line semimetal state of ZrPtGe are quite robust to changes in the exchange-correlation functional.

In Figs. 5(c) and 5(d), we present the topological surface states of ZrPtGe on the (010) surface obtained with the GGA and HSE functional, respectively. The nontrivial DSSs with unique saddlelike energy dispersion shown in Fig. 5(c) are the same as those presented in the main text. Similar to the bulk nodal-line structure, the DSSs obtained with HSE continue to display saddlelike energy dispersion [see Fig. 5(d)].
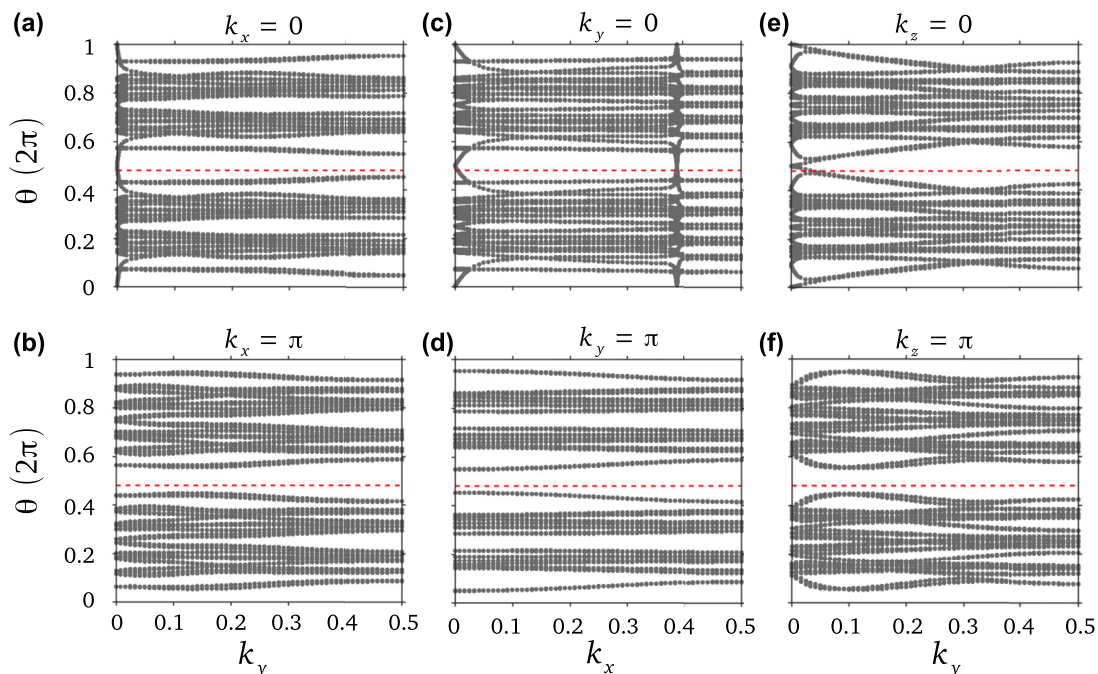

FIG. 6. Z_2 topological invariants for ZrPtGe. Evolution of Wannier charge centers (WCCs) for (a) $k_x = 0$, (b) $k_x = \pi$, (c) $k_y = 0$, (d) $k_y = \pi$, (e) $k_z = 0$, and (f) $k_z = \pi$ time-reversal invariant momentum planes. WCC evolution lines cross an arbitrary reference line (red broken line) an odd number of times on the $k_i = 0$ plane, resulting in $Z_2 = 1$.
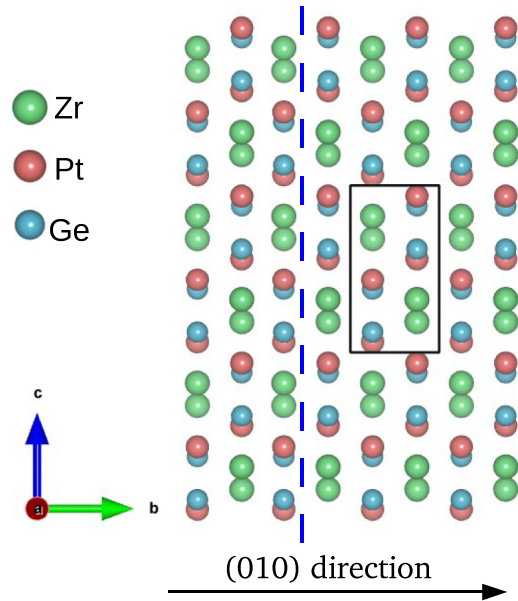
FIG. 7. Single surface termination along the (010) direction in ZrPtGe, which is marked with the dashed blue line. Black rectangle encloses the bulk unit cell in the yz plane.

APPENDIX B: NONTRIVIAL BAND TOPOLOGY

Here we present calculations of nontrivial topological invariants of ZrPtGe in the presence of SOC. As discussed in the main text, ZrPtGe is a nontrivial semimetal with $Z_2 = (1; 000)$ without the SOC. While the semimetal state is maintained

when the SOC is included with the presence of electron and hole pockets at the Fermi level, the SOC separates valence and conduction bands at all crossings points and opens a continuous band gap between valence and conduction states (see Figs. 1 and 2). The $Z_2 = (\nu_0; \nu_1\nu_2\nu_3)$ topological invariants can still be determined as in a fully gapped insulator. Figure 6 shows the evolution of Wannier charge centers (WCCs) in the six time-reversal invariant momentum planes in the bulk BZ of ZrPtGe. The WCCs have nontrivial connectivity in $k_i = 0$ planes with Z_2 index 1, while they are connected trivially in $k_i = \pi$ planes with $Z_2 = 0$, leading to $Z_2 = (1; 000)$ or a strong topological insulator phase in ZrPtGe.

APPENDIX C: ROBUSTNESS OF SADDLELIKE TOPOLOGICAL SURFACE STATES

ZrPtGe has a layered crystal structure along the (010) direction with two repeated atomic layers (see Fig. 7). Each atomic layer contains all three constituent atoms (Zr, Pt, and Ge). These two atomic layers are related via $\{C_{2y}|0\frac{1}{2}0\}$. Unlike TlBiSe$_2$ [60], if we consider only a flat surface, there is only one surface termination, which is highlighted by the broken blue line in Fig. 7. This is the surface termination we use in our calculations.

We have examined the robustness of topological surface states and their saddlelike dispersion in ZrPtGe within the framework of our tight-binding Hamiltonians by including an additional surface potential energy (SPE) as an on-site energy parameter, which is added to all the atoms in the surface layer. Figures 8 and 9 present the results obtained by changing the
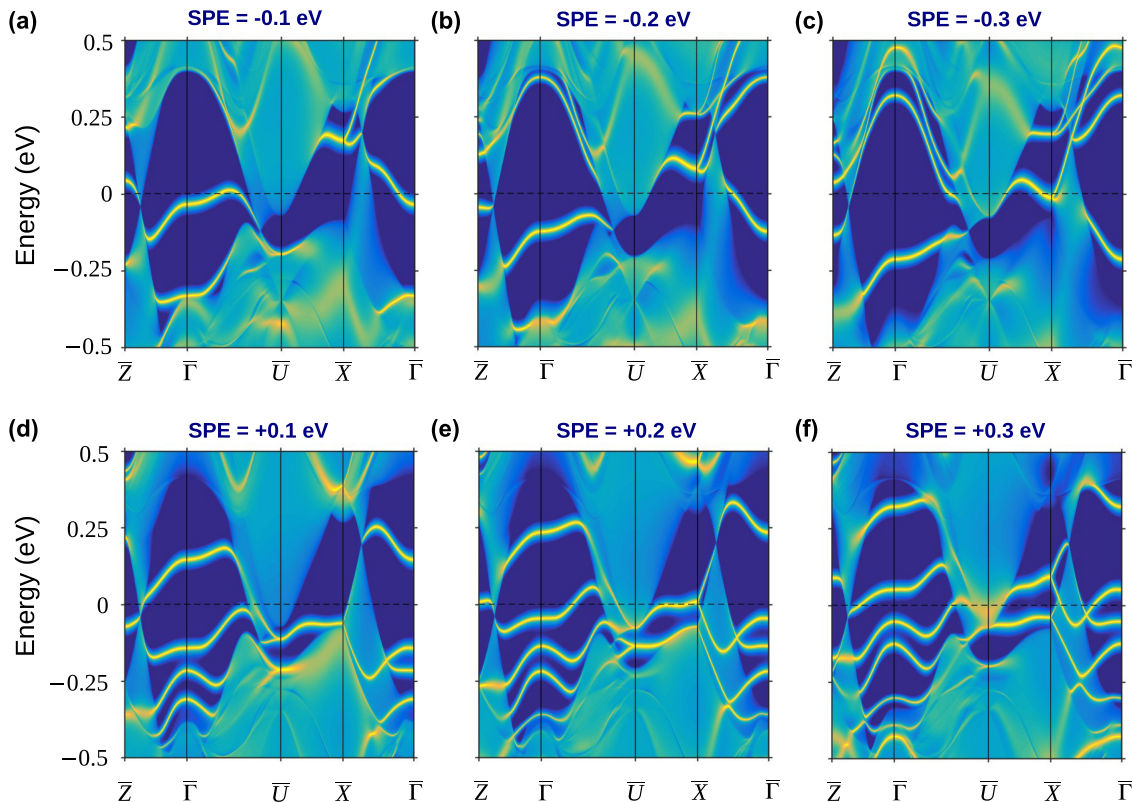

FIG. 8. Surface states of ZrPtGe (without SOC) obtained with different values of the surface potential-energy (SPE) parameter: (a) -0.1 eV, (b) -0.2 eV, (c) -0.3 eV, (d) $+0.1$ eV, (e) $+0.2$ eV, and (f) $+0.3$ eV.
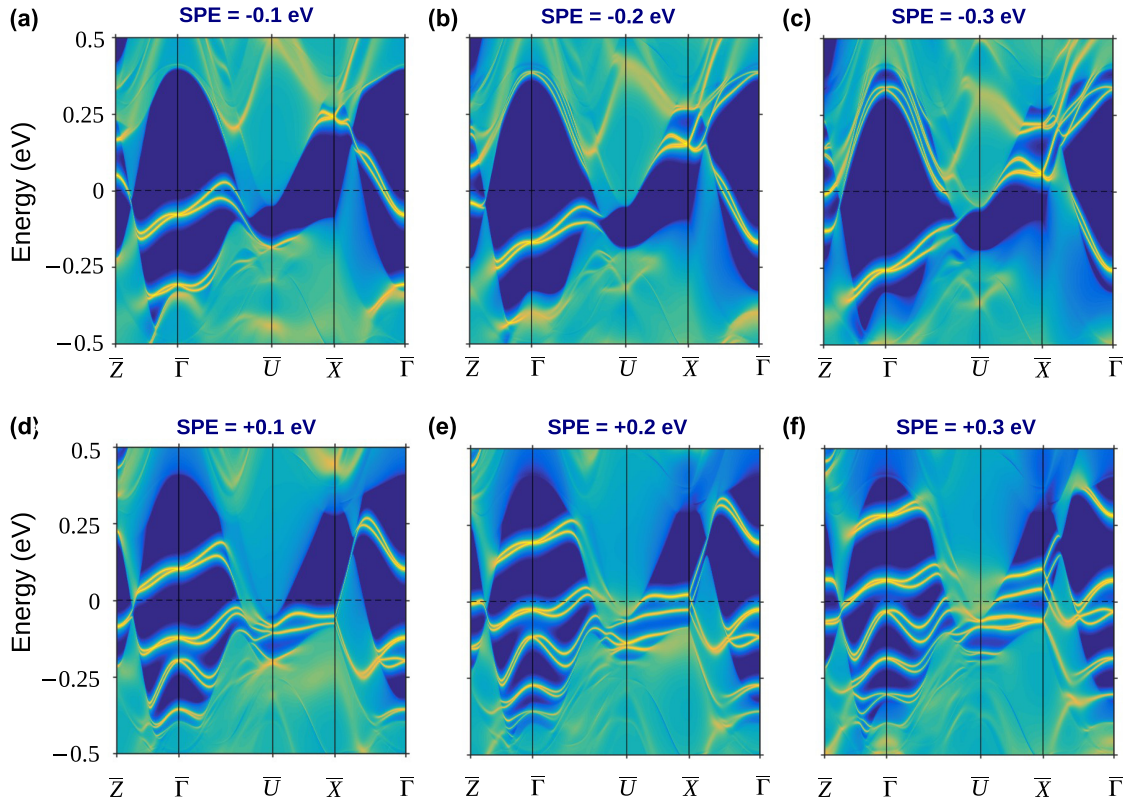
FIG. 9. Same as the caption of Fig. 8, except that this figure refers to results in which the SOC is included.

SPE from -0.3 to $+0.3$ eV for our GGA-based tight-binding Hamiltonian. Although the surface states shift towards the bulk valence or conduction bands depending on the sign of the SPE parameter, we see that the saddlelike dispersion of the surface states remains unchanged. These saddlelike surface states can be removed if they hybridize with the bulk bands, which occurs

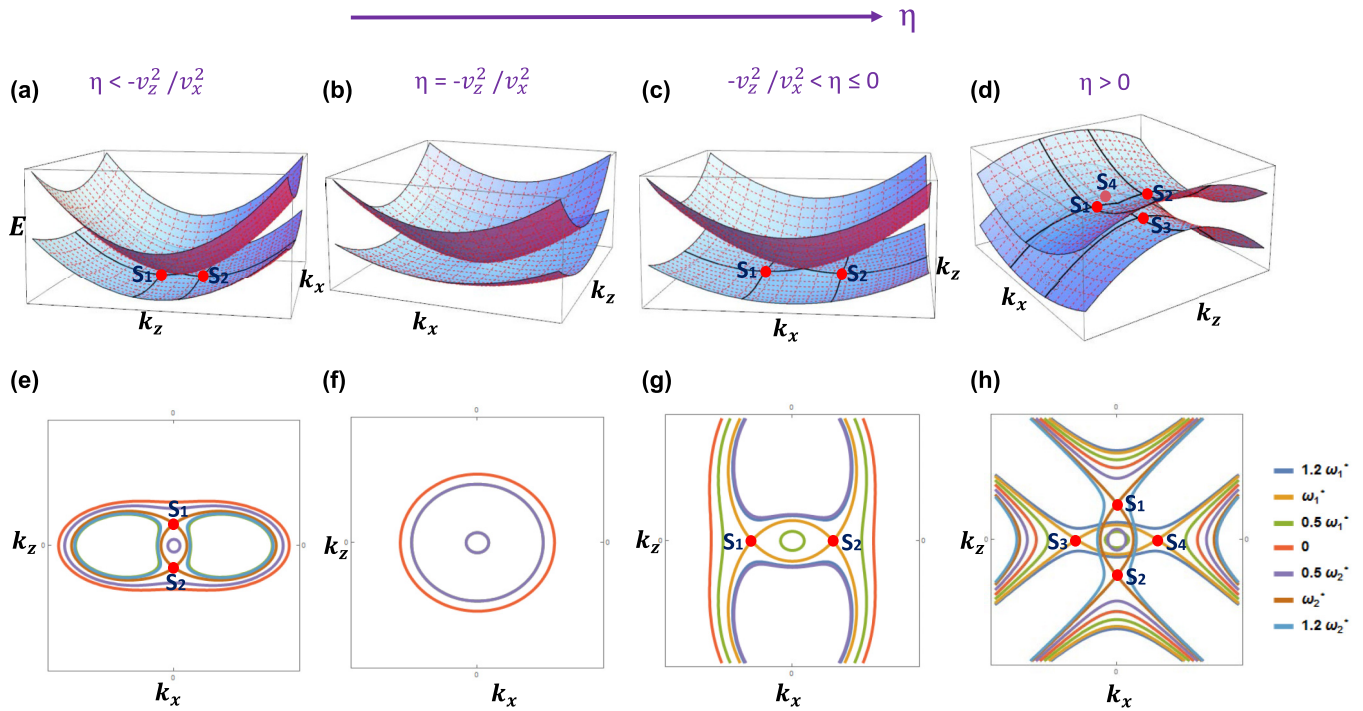FIG. 10. Transitions in surface states as a function of the parameter η. (a)–(b) Energy dispersions and (e)–(h) the associated isoenergy-band contours for the Hamiltonian $H_{\mathrm{soc}}(k_x, k_z)$; η values are given in the top row. VHSs (S_1, S_2, S_3, and S_4, shown by red dots) emerge in pairs on the k_x or k_z axis for $\eta \neq -v_z^2/v_x^2$ (see text for details).
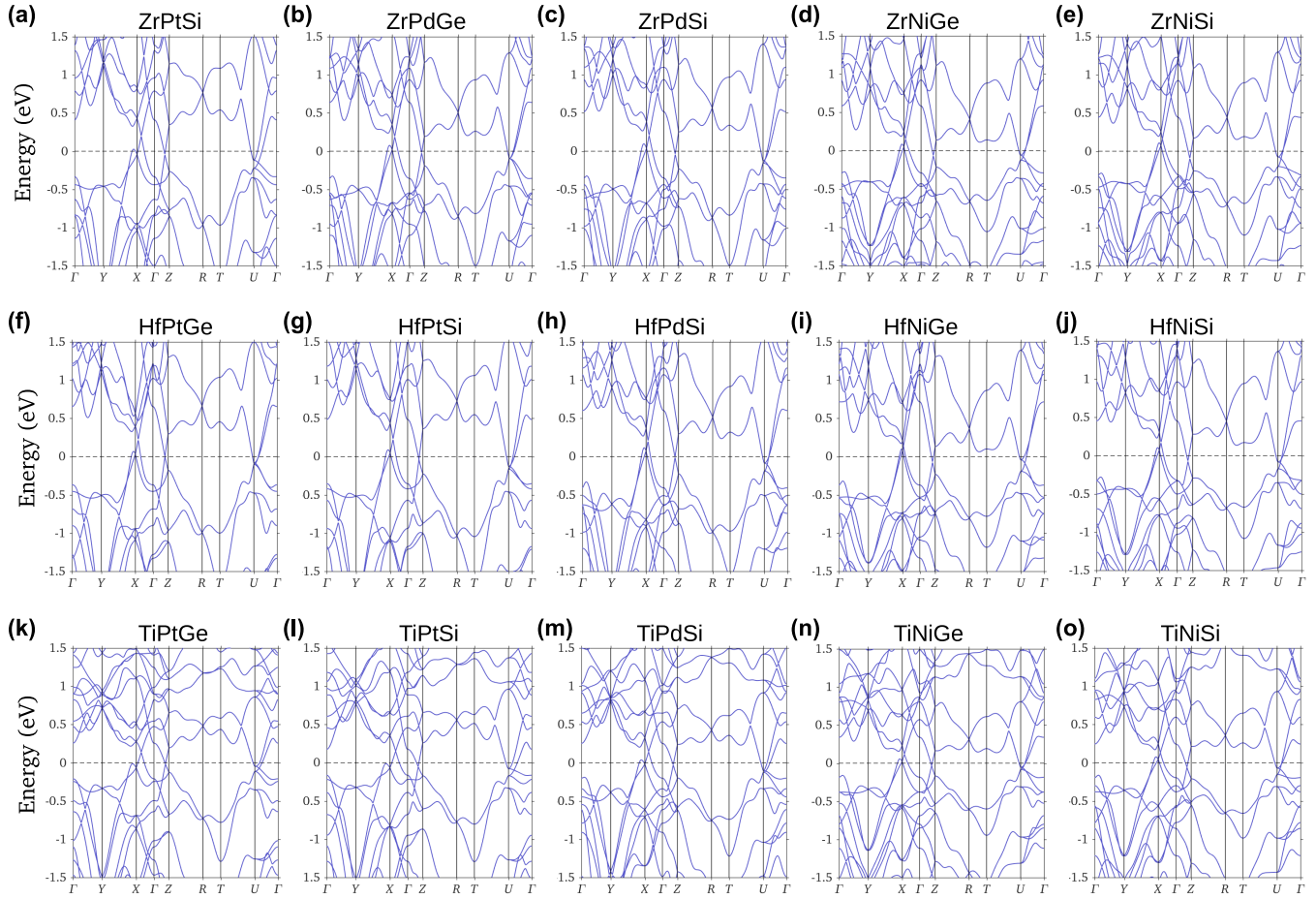
FIG. 11. Bulk band structures of the $TT'X$ family (without SOC). (a) ZrPtSi, (b) ZrPdGe, (c) ZrPdSi, (d) ZrNiGe, (e) ZrNiSi, (f) HfPtGe, (g) HfPtSi, (h) HfPdSi (i) HfNiGe, (j) HfNiSi, (k) TiPtGe, (l) TiPtSi, (m) TiPdSi, (n) TiNiGe, and (o) TiNiSi.

for large values of the SPE ($\sim \pm 0.4$ eV), much like the Dirac surface states in Bi_2Se_3. Similar results are obtained when we consider effects of the value of the SPE parameter on our HSE-based tight-binding Hamiltonian. These results show clearly that the TSSs with saddlelike dispersion in ZrPtGe are robust against variations in the surface potential.

APPENDIX D: MODEL HAMILTONIAN FOR THE (010) SURFACE STATES

The effective $\boldsymbol{k} \cdot \boldsymbol{p}$ model Hamiltonian for the saddlelike TSSs in the presence of the SOC and the corresponding energy dispersion given in Eqs. (2) and (3) are

$$H_{\text{SOC}}(k_x, k_z) = \frac{1}{2m^*}\left(k_x^2 - \eta k_z^2\right) + v_k(k_z \sigma_x - k_x \sigma_z) - v_k' k_z \sigma_y,$$
$$\text{(D1)}$$

$$E_{\pm}(\mathbf{k}) = \frac{1}{2m^*}\left(k_x^2 - \eta k_z^2\right) \pm \sqrt{v_x^2 k_x^2 + v_z^2 k_z^2}. \quad \text{(D2)}$$

Here, $v_x = v_k = v_0(1 + \alpha k^2)$ and $v_z = \sqrt{v_k^2 + v_k'^2} = v_{z0}(1 + \alpha k^2)$ are the Dirac velocities along the x and z axis, respectively, including a second-order correction. The first and second terms in Eq. (D1) describe the kinetic energy and the Rashba SOC, respectively. The third term arises from

the lowered symmetry group of the (010) surface. Its origin can be understood by recalling how the SOC comes about. When an electron with momentum $\mathbf{k}$ moves in an electric field $\mathbf{E}$, it experiences a magnetic field $\mathbf{B}_{\text{eff}} \sim \mathbf{E} \times \mathbf{k}/mc^2$ in its rest frame. This gives rise to a momentum-dependent Zeeman interaction or the SOC, $\hat{H}_{\text{SO}} \sim \mu_B(\mathbf{E} \times \mathbf{k}) \cdot \sigma/mc^2$. In a crystal, the electric field is given by the gradient of the crystal potential $\mathbf{E} = -\nabla V$ [63].

For a 2D system with C_{2v} symmetry, Vasko [61] and Bychkov and Rashba [62] showed that the interfacial electric field perpendicular to the surface, $\mathbf{E} = E_z\hat{\mathbf{z}}$, gives rise to the SOC of the form $\hat{H}_R = \frac{\alpha_R}{\hbar}(\hat{\mathbf{z}} \times \mathbf{k}) \cdot \sigma = \frac{\alpha_R}{\hbar}(k_x\sigma_y - k_y\sigma_x)$, where α_R is called the Rashba parameter. In ZrPtGe, the bulk system respects a twofold screw rotation symmetry, $\{C_{2y}|0\frac{1}{2}0\}$, which yields two symmetry related surface terminations on the (010) surface. However, for either surface termination, the symmetry is lowered to C_s with only one glide mirror plane $\{M_z|\frac{1}{2}0\frac{1}{2}\}$. This allows an interfacial electric field $\mathbf{E} = (E_x, E_y, 0)$ and results in the survival of the third term in Eq. (D1) on the surface. It should be noted that for the other surface termination, the sign of the third term in Eq. (D1) is reversed.

We now discuss the classification of saddle points and possible Lifshitz transitions resulting from variations in η based on our model Hamiltonian. As noted above as well as in the main text, the first-principles (010) surface of ZrPtGe
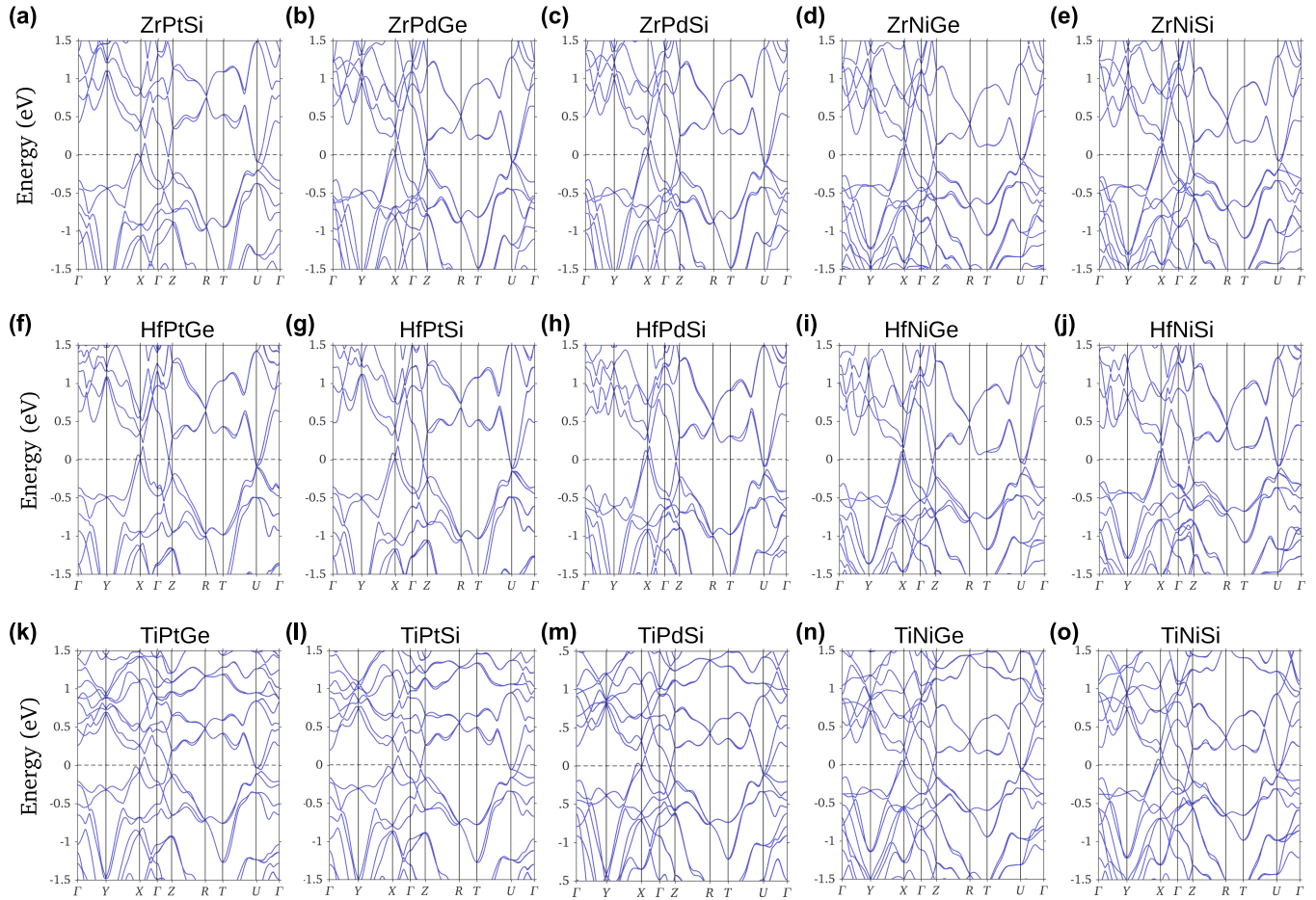
FIG. 12. Same as the caption to Fig. 11, except that this figure refers to band structure with SOC.

supports the presence of unique surface states with a saddlelike dispersion, which is described by $\eta > 0$ in our model Hamiltonian. Without SOC, $\eta > 0$ guarantees a saddle-point VHS at Γ. Moreover, when the SOC is included, $\eta > 0$ induces two pairs of type-II VHSs on the k_x and k_z axis. Note that VHSs in ZrPtGe can only appear on the k_x or k_z axis due to the constraints of C_s and time-reversal symmetries.

In Fig. 10, we demonstrate a general classification of the saddle-point VHSs as a function of η for a 2D system with C_n for $n \leqslant 2$, taking linear SOC terms into account. $\eta = -v_z^2/v_x^2$ gives a typical Rashba-like parabolic energy dispersion without a saddle-point VHS. However, for $\eta > -v_z^2/v_x^2$, one pair of saddle-point VHSs appears on the x axis at $(k_x, k_z) = (\pm m^* v_x, 0)$ with energy $\omega_1^* = -\frac{m^* v_x^2}{2}$. For $\eta < -v_z^2/v_x^2$ or $\eta > 0$, one pair of VHSs emerges on the z axis at $(k_x, k_z) = (0, \pm m^* v_z/\eta)$ with energy $\omega_2^* = \frac{m^* v_z^2}{2\eta}$. In other words, if $\eta \leqslant 0$ (excepting $\eta = -v_z^2/v_x^2$), one pair of saddle-point VHSs can still be induced by the SOC. Note, however, that this is a consequence of the SOC, so that no saddle-point VHSs can appear in the absence of the SOC for $\eta \leqslant 0$. Finally, for $\eta > 0$, two pairs of saddle-point VHSs emerge with one pair lying on the x axis and the other on the z axis, as is the case in ZrPtGe.

For a 2D system (xz plane) with n-fold rotation symmetry about the y axis, C_{ny}, for $n \geqslant 2$, the allowed linear SOC terms are $i^\lambda v_\lambda (k_+ \sigma_- + (-1)^\lambda k_- \sigma_+)$, where $\lambda = 0$ or 1. Here, C_{ny}

sends $\sigma_\pm \rightarrow e^{\pm i \frac{2\pi}{n}} \sigma_\pm$ and $k_\pm \rightarrow e^{\pm i \frac{2\pi}{n}} k_\pm$, where $k_\pm = k_z \pm i k_x$ and $\sigma_\pm = \sigma_z \pm i \sigma_x$. The presence of additional crystalline symmetries drives the SOC term into taking the form of the

TABLE I. Lattice constants a, b, and c used in our calculations and the Z_2 invariants for all 16 members of the $T T' X$ family of compounds. The lattice parameters are taken from experimental studies [55,56].

Compound	a (Å)	b (Å)	c (Å)	Z_2
ZrPtGe	6.658	3.975	7.665	(1;000)
ZrPdGe	6.677	3.954	7.702	(1;000)
ZrNiGe	6.553	3.883	7.360	(1;000)
ZrPtSi	6.597	3.902	7.539	(1;000)
ZrPdSi	6.590	3.890	7.570	(1;000)
ZrNiSi	6.470	3.815	7.263	(1;000)
TiPtGe	6.371	3.857	7.537	(1;000)
TiNiGe	6.244	3.747	7.147	(1;000)
TiPtSi	6.336	3.802	7.337	(1;000)
TiPdSi	6.324	3.779	7.394	(1;000)
TiNiSi	6.139	3.661	7.006	(1;000)
HfPtGe	6.603	3.950	7.617	(1;000)
HfNiGe	6.500	3.810	7.290	(1;000)
HfPtSi	6.550	3.881	7.505	(1;000)
HfPdSi	6.570	3.874	7.675	(1;000)
HfNiSi	6.390	3.890	7.200	(1;000)

Rashba SOC, $v_1(k_z\sigma_x - k_x\sigma_z)$ for $\lambda = 1$ (C_{nv} symmetry, for example) and $v_0(k_z\sigma_z + k_x\sigma_x)$ for $\lambda = 0$ (e.g., D_n symmetry), and both v_0 and v_1 terms are allowed (e.g., C_n symmetry). Note that according to Eq. (D2) in all cases $v_z^2 = v_x^2$ ($= v_1^2$, or v_0^2, or $v_0^2 + v_1^2$), resulting in the critical point $-v_z^2/v_x^2 = -1$. For $n > 2$, however, η is not allowed to take any other value than -1. This clearly shows that a system with $C_{ny}(n > 2)$ can only support Rashba-like parabolic energy dispersion for the surface state when only linear SOC terms are considered.

APPENDIX E: BAND STRUCTURE OF THE $TT'X$ FAMILY

Figures 11 and 12 present the bulk band structures of all members of the $TT'X$ family without and with SOC. The 16 members in this family are listed in Table I along with the lattice constants [55,56] used in our calculations and their topological invariants (with SOC). All these compounds host single nodal lines (without SOC) with substantial dispersions similar to ZrPtGe. Inclusion of SOC gaps the nodal line in all cases and yields the topological insulator state with $Z_2 = (1;000)$. A reference to the band structures, however, shows that the area occupied by the nodal loop on the $k_y = 0$ plane of the bulk BZ depends on the transition-metal element involved. This is also the case with the details of band crossings at the high-symmetry points above and below the Fermi level (see Figs. 11 and 12). These results show that the $TT'X$ family offers an interesting materials platform where the electronic structure can be tuned through the choice of the transition-metal element.

[1] A. Bansil, H. Lin, and T. Das, Colloquium: Topological band theory, Rev. Mod. Phys. **88**, 021004 (2016).

[2] M. Z. Hasan, S.-Y. Xu, and G. Bian, Topological insulators, topological superconductors and Weyl fermion semimetals: discoveries, perspectives and outlooks, Phys. Scr. **2015**, 014001 (2015).

[3] L. Balents, Viewpoint: Weyl electrons kiss, Physics **4**, 36 (2011).

[4] A. M. Turner and A. Vishwanath, *Beyond Band Insulators: Topology of Semimetals and Interacting Phases* (Elsevier, New York, 2013).

[5] X. Wan, A. M. Turner, A. Vishwanath, and S. Y. Savrasov, Topological semimetal and Fermi-arc surface states in the electronic structure of pyrochlore iridates, Phys. Rev. B **83**, 205101 (2011).

[6] B. Singh, A. Sharma, H. Lin, M. Z. Hasan, R. Prasad, and A. Bansil, Topological electronic structure and Weyl semimetal in the TlBiSe$_2$ class of semiconductors, Phys. Rev. B **86**, 115208 (2012).

[7] S.-M. Huang, S.-Y. Xu, I. Belopolski, C.-C. Lee, G. Chang, B. Wang, N. Alidoust, G. Bian, M. Neupane, C. Zhang, S. Jia, A. Bansil, H. Lin, and M. Z. Hasan, A Weyl fermion semimetal with surface Fermi arcs in the transition metal monopnictide TaAs class, Nat. Commun. **6**, 7373 (2015).

[8] H. Weng, C. Fang, Z. Fang, B. A. Bernevig, and X. Dai, Weyl semimetal phase in noncentrosymmetric transition-metal monophosphides, Phys. Rev. X **5**, 011029 (2015).

[9] S.-Y. Xu, I. Belopolski, N. Alidoust, M. Neupane, G. Bian, C. Zhang, R. Sankar, G. Chang, Z. Yuan, C.-C. Lee, S.-M. Huang, H. Zheng, J. Ma, D. S. Sanchez, B. Wang, A. Bansil, F. Chou, P. P. Shibayev, H. Lin, S. Jia, and M. Z. Hasan, Discovery of a Weyl fermion semimetal and topological Fermi arcs, Science **349**, 613 (2015).

[10] B. Q. Lv, H. M. Weng, B. B. Fu, X. P. Wang, H. Miao, J. Ma, P. Richard, X. C. Huang, L. X. Zhao, G. F. Chen, Z. Fang, X. Dai, T. Qian, and H. Ding, Experimental Discovery of Weyl Semimetal TaAs, Phys. Rev. X **5**, 031013 (2015).

[11] Z. K. Liu, B. Zhou, Y. Zhang, Z. J. Wang, H. M. Weng, D. Prabhakaran, S.-K. Mo, Z. X. Shen, Z. Fang, X. Dai, Z. Hussain, and Y. L. Chen, Discovery of a three-dimensional topological Dirac semimetal, Na$_3$Bi, Science **343**, 864 (2014).

[12] Z. K. Liu, J. Jiang, B. Zhou, Z. J. Wang, Y. Zhang, H. M. Weng, D. Prabhakaran, S.-K. Mo, H. Peng, P. Dudin, T. Kim, M. Hoesch, Z. Fang, X. Dai, Z. X. Shen, D. L. Feng, Z. Hussain, and Y. L. Chen, A stable three-dimensional topological Dirac semimetal Cd$_3$As$_2$, Nat. Mater. **13**, 677 (2014).

[13] C. Fang, H. Weng, X. Dai, and Z. Fang, Topological nodal line semimetals, Chin. Phys. B **25**, 117106 (2016).

[14] A. A. Burkov, M. D. Hook, and L. Balents, Topological nodal semimetals, Phys. Rev. B **84**, 235126 (2011).

[15] M. Phillips and V. Aji, Tunable line node semimetals, Phys. Rev. B **90**, 115111 (2014).

[16] C.-K. Chiu and A. P. Schnyder, Classification of reflection-symmetry-protected topological semimetals and nodal superconductors, Phys. Rev. B **90**, 205136 (2014).

[17] C. Fang, Y. Chen, H.-Y. Kee, and L. Fu, Topological nodal line semimetals with and without spin-orbital coupling, Phys. Rev. B **92**, 081201 (2015).

[18] L. Huang, T. M. McCormick, M. Ochi, Z. Zhao, M.-T. Suzuki, R. Arita, Y. Wu, D. Mou, H. Cao, J. Yan, N. Trivedi, and A. Kaminski, Spectroscopic evidence for a type II Weyl semimetallic state in MoTe$_2$, Nat. Mater. **15**, 1155 (2016).

[19] I. Belopolski, S.-Y. Xu, Y. Ishida, X. Pan, P. Yu, D. S. Sanchez, H. Zheng, M. Neupane, N. Alidoust, G. Chang, T.-R. Chang, Y. Wu, G. Bian, S.-M. Huang, C.-C. Lee, D. Mou, L. Huang, Y. Song, B. Wang, G. Wang, Y.-W. Yeh, N. Yao, J. E. Rault, P. Le Fèvre, F. M. C. Bertran, H.-T. Jeng, T. Kondo, A. Kaminski, H. Lin, Z. Liu, F. Song, S. Shin, and M. Z. Hasan, Fermi arc electronic structure and Chern numbers in the type-II Weyl semimetal candidate Mo$_x$W$_{1-x}$Te$_2$, Phys. Rev. B **94**, 085127 (2016).

[20] M. N. Ali, J. Xiong, S. Flynn, J. Tao, Q. D. Gibson, L. M. Schoop, T. Liang, N. Haldolaarachchige, M. Hirschberger, N. P. Ong, and R. J. Cava, Large, non-saturating magnetoresistance in WTe2, Nature (London) **514**, 205 (2014).

[21] S.-Y. Xu, N. Alidoust, G. Chang, H. Lu, B. Singh, I. Belopolski, D. Sanchez, X. Zhang, G. Bian, H. Zheng, M.-A. Husanu, Y. Bian, S.-M. Huang, C.-H. Hsu, T.-R. Chang, H.-T. Jeng, A. Bansil, V. N. Strocov, H. Lin, S. Jia, and M. Z. Hasan, Discovery of Lorentz-violating Weyl fermion semimetal state in LaAlGe materials, Sci. Adv. **3**, e1603266 (2017).

[22] Z. Yan and Z. Wang, Tunable Weyl Points in Periodically Driven Nodal Line Semimetals, Phys. Rev. Lett. **117**, 087402 (2016).

[23] N. B. Kopnin, T. T. Heikkilä, and G. E. Volovik, High-temperature surface superconductivity in topological flat-band systems, Phys. Rev. B **83**, 220503 (2011).

[24] Y. Huh, E.-G. Moon, and Y. B. Kim, Long-range Coulomb interaction in nodal-ring semimetals, Phys. Rev. B **93**, 035138 (2016).

[25] J. Liu and L. Balents, Correlation effects and quantum oscillations in topological nodal-loop semimetals, Phys. Rev. B **95**, 075426 (2017).

[26] Y. Kim, B. J. Wieder, C. L. Kane, and A. M. Rappe, Dirac Line Nodes in Inversion-Symmetric Crystals, Phys. Rev. Lett. **115**, 036806 (2015).

[27] R. Yu, H. Weng, Z. Fang, X. Dai, and X. Hu, Topological Node-Line Semimetal and Dirac Semimetal State in Antiperovskite Cu_3PdN, Phys. Rev. Lett. **115**, 036807 (2015).

[28] A. Yamakage, Y. Yamakawa, Y. Tanaka, and Y. Okamoto, Line-node Dirac semimetal and topological insulating phase in noncentrosymmetric pnictides CaAgX (X = P, As), J. Phys. Soc. Jpn. **85**, 013708 (2016).

[29] Y.-H. Chan, C.-K. Chiu, M. Y. Chou, and A. P. Schnyder, Ca_3P_2 and other topological semimetals with line nodes and drumhead surface states, Phys. Rev. B **93**, 205132 (2016).

[30] L. Lu, L. Fu, J. D. Joannopoulos, and M. Soljacic, Weyl points and line nodes in gyroid photonic crystals, Nat. Photon. **7**, 294 (2013).

[31] G. Bian, T.-R. Chang, H. Zheng, S. Velury, S.-Y. Xu, T. Neupert, C.-K. Chiu, S.-M. Huang, D. S. Sanchez, I. Belopolski, N. Alidoust, P.-J. Chen, G. Chang, A. Bansil, H.-T. Jeng, H. Lin, and M. Z. Hasan, Drumhead surface states and topological nodal-line fermions in $TlTaSe_2$, Phys. Rev. B **93**, 121113 (2016).

[32] J.-T. Wang, H. Weng, S. Nie, Z. Fang, Y. Kawazoe, and C. Chen, Body-Centered Orthorhombic C_{16}: A Novel Topological Node-Line Semimetal, Phys. Rev. Lett. **116**, 195501 (2016).

[33] K. Mullen, B. Uchoa, and D. T. Glatzhofer, Line of Dirac Nodes in Hyperhoneycomb Lattices, Phys. Rev. Lett. **115**, 026403 (2015).

[34] H. Huang, J. Liu, D. Vanderbilt, and W. Duan, Topological nodal-line semimetals in alkaline-earth stannides, germanides, and silicides, Phys. Rev. B **93**, 201114 (2016).

[35] M. Neupane, I. Belopolski, M. M. Hosen, D. S. Sanchez, R. Sankar, M. Szlawska, S.-Y. Xu, K. Dimitri, N. Dhakal, P. Maldonado, P. M. Oppeneer, D. Kaczorowski, F. Chou, M. Z. Hasan, and T. Durakiewicz, Observation of topological nodal fermion semimetal phase in ZrSiS, Phys. Rev. B **93**, 201104 (2016).

[36] L. M. Schoop, M. N. Ali, C. Straber, A. Topp, A. Varykhalov, D. Marchenko, V. Duppel, S. S. P. Parkin, B. V. Lotsch, and C. R. Ast, Dirac cone protected by non-symmorphic symmetry and three-dimensional Dirac line node in ZrSiS, Nat. Commun. **7**, 11696 (2016).

[37] G. Bian, T.-R. Chang, R. Sankar, S.-Y. Xu, H. Zheng, T. Neupert, C.-K. Chiu, S.-M. Huang, G. Chang, I. Belopolski, D. S. Sanchez, M. Neupane, N. Alidoust, C. Liu, B. Wang, C.-C. Lee, H.-T. Jeng, C. Zhang, Z. Yuan, S. Jia, A. Bansil, F. Chou, H. Lin, and M. Z. Hasan, Topological nodal-line fermions in spin-orbit metal PbTaSe2, Nat. Commun. **7**, 10556 (2016).

[38] Y. Wu, L.-L. Wang, E. Mun, D. D. Johnson, D. Mou, L. Huang, Y. Lee, S. L. Bud'ko, P. C. Canfield, and A. Kaminski, Dirac node arcs in PtSn4, Nat. Phys. **12**, 667 (2016).

[39] Y. Xia, D. Qian, D. Hsieh, L. Wray, A. Pal, H. Lin, A. Bansil, D. Grauer, Y. S. Hor, R. J. Cava, and M. Z. Hasan, Observation of a large-gap topological-insulator class with a single Dirac cone on the surface, Nat. Phys. **5**, 398 (2009).

[40] L. Fu, Hexagonal Warping Effects in the Surface States of the Topological Insulator Bi_2Te_3, Phys. Rev. Lett. **103**, 266801 (2009).

[41] L. Van Hove, The Occurrence of singularities in the elastic frequency distribution of a crystal, Phys. Rev. **89**, 1189 (1953).

[42] W. Kohn and J. M. Luttinger, New Mechanism for Superconductivity, Phys. Rev. Lett. **15**, 524 (1965).

[43] C. Honerkamp and M. Salmhofer, Magnetic and Superconducting Instabilities of the Hubbard Model at the Van Hove Filling, Phys. Rev. Lett. **87**, 187004 (2001).

[44] R. Hlubina, S. Sorella, and F. Guinea, Ferromagnetism in the Two Dimensional $t - t'$ Hubbard Model at the Van Hove Density, Phys. Rev. Lett. **78**, 1343 (1997).

[45] A. Ziletti, S. M. Huang, D. F. Coker, and H. Lin, Van Hove singularity and ferromagnetic instability in phosphorene, Phys. Rev. B **92**, 085423 (2015).

[46] H. Yao and F. Yang, Topological odd-parity superconductivity at type-II two-dimensional van Hove singularities, Phys. Rev. B **92**, 035132 (2015).

[47] B. Singh, C.-H. Hsu, W.-F. Tsai, V. M. Pereira, and H. Lin, Stable charge density wave phase in a 1T-TiSe$_2$ monolayer, Phys. Rev. B **95**, 245136 (2017).

[48] P. Hohenberg and W. Kohn, Inhomogeneous Electron Gas, Phys. Rev. **136**, B864 (1964).

[49] G. Kresse and J. Furthmüller, Efficient iterative schemes for *ab initio* total-energy calculations using a plane-wave basis set, Phys. Rev. B **54**, 11169 (1996).

[50] G. Kresse and D. Joubert, From ultrasoft pseudopotentials to the projector augmented-wave method, Phys. Rev. B **59**, 1758 (1999).

[51] J. P. Perdew, K. Burke, and M. Ernzerhof, Generalized Gradient Approximation Made Simple, Phys. Rev. Lett. **77**, 3865 (1996).

[52] N. Marzari and D. Vanderbilt, Maximally localized generalized Wannier functions for composite energy bands, Phys. Rev. B **56**, 12847 (1997).

[53] Q. Wu, S. Zhang, H.-F. Song, M. Troyer, and A. A. Soluyanov, WannierTools : An open-source software package for novel topological materials, Comput. Phys. Commun. **224**, 405 (2018).

[54] M. P. L. Sancho, J. M. L. Sancho, J. M. L. Sancho, and J. Rubio, Highly convergent schemes for the calculation of bulk and surface Green functions, J. Phys. F **15**, 851 (1985).

[55] S.-V. Ackerbauer, R. Gumeniuk, Y. Prots, H. Borrmann, F. Weitzer, and A. Leithe-Jasper, Crystal structures of zirconium-platinum-silicon (1 : 1 : 1), ZrPtSi, zirconium-platinum-germanium (1 : 1 : 1), ZrPtGe and titanium-platinum-silicon (1 : 1 : 1), TiPtSi, Z. Kristallogr. NCS **225**, 7 (2010).

[56] C. Benndorf, H. Eckert, and R. Pottgen, 29Si, 47Ti, 49Ti and 195Pt solid state MAS NMR spectroscopic investigations of ternary silicides TPtSi, germanides TPtGe (T = Ti, Zr, Hf) and stannide TiPtSn, Dalton Trans. **45**, 8215 (2016).

[57] Y. Nagata, K. Sodeyama, S. Yashiro, H. Sasaki, H. Samata, T. Uchida, and M. Lan, New intermetallic compounds found in Hf-Ni-Ge and Hf-Pt-Ge systems, J. Alloys Compd. **281**, 112 (1998).

[58] S. Yashiro, Y. Nagata, H. Samata, and S. Abe, Magnetism and transport properties of HfMSi (M=Pt, Pd) and HfRh$_{1x}$Pd$_x$Si, J. Alloys Compd. **298**, 51 (2000).

[59] J. Heyd, G. E. Scuseria, and M. Ernzerhof, Hybrid functionals based on a screened Coulomb potential, J. Chem. Phys. **118**, 8207 (2003).

[60] B. Singh, H. Lin, R. Prasad, and A. Bansil, Role of surface termination in realizing well-isolated topological surface states within the bulk band gap in TlBiSe$_2$ and TlBiTe$_2$, Phys. Rev. B **93**, 085113 (2016).

[61] F. T. Vasko, Spin splitting in the spectrum of two-dimensional electrons due to the surface potential, Pis'ma Zh. Eksp. Teor. Fiz. **30**, 574 (1979).

[62] Y. A. Bychkov, and E. I. Rashba, Properties of a 2D electron gas with lifted spectral degeneracy, Pis'ma Zh. Eksp. Teor. Fiz. **39**, 66 (1984).

[63] A. Manchon, H. C. Koo, J. Nitta, S. M. Frolov, and R. A. Duine, New perspectives for Rashba spin-orbit coupling, Nat. Mater. **14**, 871 (2015).